

3C 223.1: A source with unusual spectral properties

Dharam Vir Lal[★] and A. Pramesh Rao[★]

National Centre for Radio Astrophysics (NCRA–TIFR), Pune University campus, Ganeshkhind, Pune 411 007, India

Accepted 2004 September 23. Received 2004 September 13; in original form 2004 July 23

ABSTRACT

Analysis of Giant Metrewave Radio Telescope low-frequency data for an *X*-shaped source, 3C 223.1, has revealed an unusual result. The radio morphologies of it at 240 and 610 MHz show a well defined *X* shape with a pair of active jets along the north–south axis and a pair of wings along the east–west axis, which pass symmetrically through the undetected radio core. The wings (or low-surface-brightness jets) have flatter spectral indices with respect to the high-surface-brightness jets; this confirms the earlier marginal result obtained at high frequency by Dennett-Thorpe et al. (2002). Although unusual, it is a valuable result which puts stringent constraints on the formation models and the nature of these sources. This result clearly shows the value of mapping the sample of *X*-shaped sources at low frequencies.

Key words: galaxies: active – galaxies: formation – galaxies: individual: 3C 223.1 – radio continuum: galaxies.

1 INTRODUCTION

The *X*-shaped or ‘winged’ sources form a peculiar class of extragalactic sources consisting of 11 sources compiled by Leahy & Parma (1992). These sources are characterized by two low-surface-brightness lobes (the ‘wings’) oriented at an angle to the ‘active’ (or high-surface-brightness) radio lobes, giving the total source an *X* shape; both sets of lobes usually pass symmetrically through the centre of the associated host galaxy. Recently, Merritt & Ekers (2002) noted that seven out of 11 are of Fanaroff–Riley type II (FR II) (Fanaroff & Riley 1974) and the rest are either FR I or mixed.

Source 3C 223.1 ($z = 0.1075$) is a classical *X*-shaped source which does not reside in a rich cluster; instead, it probably resides in an environment similar to ‘classical’ FR IIs of similar radio power. Although, the host galaxy seems to be a relatively undisturbed elliptical, its *Hubble Space Telescope* (*HST*) image shows a beautiful central bulge with a dusty disc (de Koff et al. 1996). Radio observations show a high degree of polarization (15–30 per cent) in the wings, and an apparent magnetic field structure parallel to the edge of the source and along the length of the wings (Dennett-Thorpe et al. 2002). Further high-frequency and high-resolution radio polarization images showed field lines wrapping around the edges, as well as complex internal structure (Black et al. 1992).

We have started a project to study the sample of *X*-shaped radio sources at 240 and 610 MHz using the Giant Metrewave Radio Telescope (GMRT). In this paper, we present results for 3C 223.1 and describe its morphological and spectral properties. We use the data to study the behaviour of the low-frequency spectra at several locations (the north and south lobes and the east and west wings) across the source and compare it with the existing models. We would

also discuss the implications of our results on the formation models of *X*-shaped sources.

2 OBSERVATIONS

The 240 and 610 MHz feeds of GMRT (Ananthakrishnan & Rao 2002) are coaxial feeds, and therefore simultaneous multifrequency observations at these two frequencies are possible. We made full-synthesis observations of 3C 223.1 at 240 and 610 MHz, in the dual frequency mode, using the GMRT on 2003 December 18 in the standard spectral line mode with a spectral resolution of 125 kHz. Table 1 gives the details of the observations. The visibility data were converted to FITS and analysed using the standard AIPS package. The flux calibrator 3C 286 was observed in the end as an amplitude calibrator and to estimate and correct for the bandpass shape. We used the flux density scale, which is an extension of the Baars et al. (1977) scale to low frequencies, using the coefficients in the AIPS task ‘SETJY’. Source 0834+555 was used as the phase calibrator and was observed once every 35 min. The error in the estimated flux density, both due to calibration and systematic, was $\lesssim 5$ per cent. The data suffered from scintillations and intermittent radio frequency interference (RFI). In addition to normal editing of the data, the scintillation-affected data and the channels affected by RFI were identified and edited, after which the central channels were averaged using the AIPS task ‘SPLAT’ to reduce the data volume. To avoid bandwidth smearing, 5.00 MHz of clean band at 240 MHz was reduced to four channels of 1.25 MHz each. At 610 MHz, where there was little RFI, 14.25 MHz of clean band was averaged to give three channels of 4.75 MHz each.

While imaging, 55 facets (obtained using the AIPS task ‘SETFC’) spread across a $\sim 2 \times 2$ deg² field were used at 240 MHz and 12 facets covering slightly less than a 0.7×0.7 deg² field were used at

[★]E-mail: dharam@ncra.tifr.res.in (DVL); pramesh@ncra.tifr.res.in (APR)

Table 1. The observing log for 3C 223.1. The centre of the field was at RA (J2000) = 09^h41^m24^s.0 and Dec. (J2000) = 39°44′41″.9.

	610 MHz	240 MHz
Observing date	2003 December 18	2003 December 18
Duration	10.45 h	10.45 h
Centre frequency	606.68 MHz	237.19 MHz
Nominal bandwidth	16 MHz	6 MHz
Effective bandwidth	14.25 MHz	5 MHz
Primary beam	43 arcmin	108 arcmin
Synthesized beam (PA)	8.6 × 5.0 arcsec ² 80°4	17.4 × 13.3 arcsec ² 80°3
Sensitivity (σ)	0.4 mJy beam ⁻¹	3.0 mJy beam ⁻¹
Dynamic range	~1700	~900
Calibrator	3C 286	3C 286
S_{ν} (3C 286)	21.02 Jy	28.07 Jy

610 MHz to map each of the two fields using AIPS task ‘IMAGR’. We used ‘uniform’ weighting and the 3D option for W-term correction throughout our analysis. The presence of a large number of point sources in the field allowed us to perform phase self-calibration to improve the image. After 2–3 rounds of phase self-calibration, a final self-calibration of both amplitude and phase was made to get the final image. At each round of self-calibration, the image and the visibilities were compared to check for the improvement in the source model. The final maps were combined using AIPS task ‘FLATN’ and corrected for the primary beam of the GMRT antennas.

The full-synthesis radio images shown in Fig. 1 have nearly complete UV coverage, angular resolution of ~15 arcsec and ~8 arcsec and rms noise of ~3.0 and ~0.4 mJy beam⁻¹ at 240 and 610 MHz, respectively. The dynamic ranges in the two maps are ~900 and ~1700 at 240 and 610 MHz, respectively. The GMRT has a hybrid configuration (Swarup et al. 1991), with 14 of its 30 antennas located in a central compact array with size ~1.1 km and the remaining antennas distributed in a roughly Y-shaped configuration, giving a maximum baseline length of ~25 km. The baselines obtained from antennas in the central square are similar in length to those of the Very Large Array (VLA) D-array, whereas the baselines between the arm antennas are comparable in length to the VLA B-array. A single observation with the GMRT hence yields information on both small and large angular scales with reasonably good sensitivity.

3 RADIO MORPHOLOGY

The first high-angular-resolution, high-sensitivity images of 3C 223.1 at the lowest frequencies of 240 MHz (upper right-hand panel) and 610 MHz (upper left-hand panel) are shown in Fig. 1. This complex radio source shows an X-shaped morphology at both 240 and 610 MHz. The angular extent is ~105 arcsec along the apparently active lobes (those with hotspots) and ~150 arcsec along the wings. The nuclear source of 3C 223.1 is invisible at both these frequencies and also in the radio maps of Dennett-Thorpe et al. (2002), but is detected and is unresolved at 8.4 GHz (Black et al. 1992). The weak jet detected midway between the core and the north lobe by Black et al. (1992) at 8.4 GHz is not seen in our low-resolution maps because of coarser resolution. Our low-resolution maps also suggest a sharp boundary at the farthest end of the north lobe and a likely ring-like feature in the south lobe, which is consistent with earlier results of Black et al. (1992).

The final calibrated UV data at 610 MHz was mapped using a UV taper of 0–22 λ , which is similar to that of the 240 MHz data,

and then restored using the restoring beam corresponding to the 240 MHz map (Fig. 1, lower left-hand panel). In Table 2, we show the integrated flux densities of 3C 223.1 along with previous measurements at other frequencies. Our estimates at both frequencies, 240 and 610 MHz, agree well with those of the measurements from other instruments. We therefore believe that we have not lost any flux density in our interferometric observations and there are no systematics introduced in our analysis.

4 LOW-FREQUENCY RADIO SPECTRA

The observations and morphology described above allow us to investigate in detail the spectral index distribution of 3C 223.1. The restored and matched maps at 240 and 610 MHz were used further for the spectral analysis. We determine the spectral index distribution using the standard direct method of determining the spectral index between maps $S_{\nu_1}(x, y)$ and $S_{\nu_2}(x, y)$ at two frequencies ν_1 and ν_2 , given by

$$\alpha_{\nu_1, \nu_2}(x, y) \equiv \frac{\log[S_{\nu_1}(x, y)/S_{\nu_2}(x, y)]}{\log(\nu_1/\nu_2)}.$$

The low-frequency flux densities plotted in Fig. 2 are calculated using the images shown in Fig. 1 (upper right-hand and lower left-hand panels), which are matched to the same resolution, and these values are tabulated in Table 2. The flux densities at higher frequencies in this table are quoted using earlier observations in Dennett-Thorpe et al. (2002). The flux densities for the active lobes and the wings are integrated over the region, which is at least 4 times the beam size and above their 3σ contour to reduce statistical errors. Analysis of the spectrum in different regions of the source shows remarkable variation across the source (Fig. 1, lower right-hand panel).

We have obtained the best power-law fit ($S_{\nu} \propto \nu^{\alpha}$). The low-frequency (240–610 MHz) fitted spectra have $-0.37 < \alpha < -1.08$ for all regions across the source. The source also shows evidence for steeper spectra in the active lobes than in the wings. The east and west wings have low-frequency (240–610 MHz) spectral indices, -0.37 ± 0.03 and -0.62 ± 0.02 respectively, whereas the north and south active lobes have -1.08 ± 0.01 and -1.08 ± 0.01 , respectively (also see Fig. 1 caption). These results at low frequencies are consistent with those obtained at high frequency by Dennett-Thorpe et al. (2002), who found the spectral indices between 1.4 and 32 GHz to be -0.70 ± 0.03 and -0.66 ± 0.03 for the east and west wings, and -0.75 ± 0.02 and -0.77 ± 0.02 for the north and south active lobes, respectively.

This result being unusual, we were worried about the possibility that the different UV coverages at 240 and 610 MHz could produce some systematic errors. Although this is unlikely, because the source is only 3–4 arcmin across and is much smaller than the primary beam, we examined the effect of different UV coverages by Fourier transforming the 240 MHz clean map, sampling it with the UV coverage of 610 MHz and re-imaging this visibility data set. The resultant map showed no systematic differences from the original 240 MHz map and the rms difference in the two maps was less than 4 per cent, corresponding to the rms error in the spectral index of $\lesssim 0.05$. Furthermore, the 240 MHz contour plot of the source (Fig. 1, upper right-hand panel) shows some evidence that this image contains a negative depression around the source that is less prominent at 610 MHz. While imaging, we did not provide zero-spacing flux density, but we have done deep cleaning, so as not to make any deconvolution errors. Nevertheless, we look into the errors that would

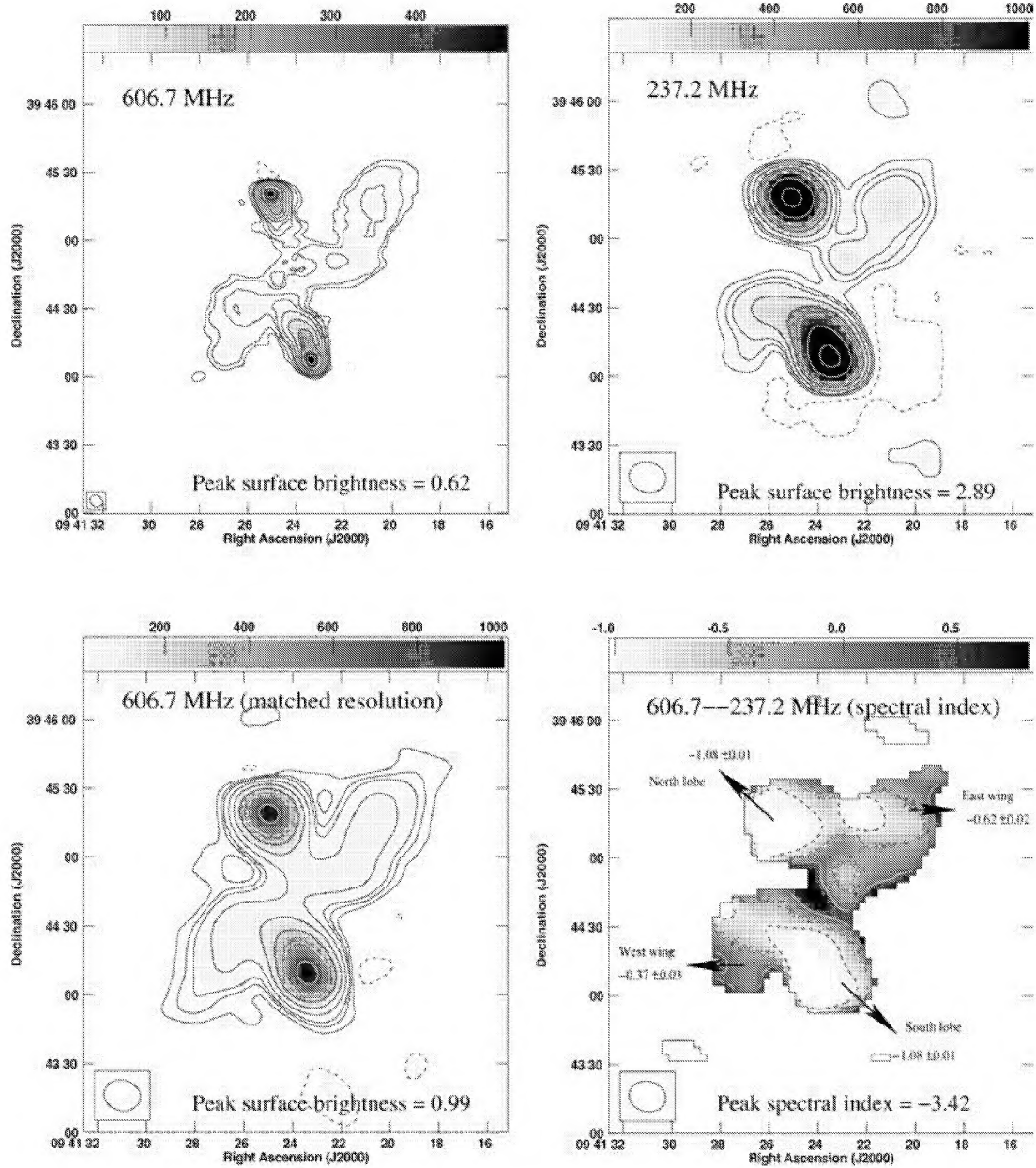


Figure 1. Upper panels: full-synthesis GMRT maps of 3C 223.1 at 610 MHz (left-hand panel) and 240 MHz (right-hand panel). The CLEAN beams for 610- and 240-MHz maps are $6.1 \times 4.8 \text{ arcsec}^2$ at a PA of $66^\circ 8'$ and $13.1 \times 10.8 \text{ arcsec}^2$ at a PA of $35^\circ 2'$, respectively. The contour levels in the two maps, respectively, are $-0.06, 0.06, 0.08, 0.16, 0.24, 0.48, 1, 2, 4, 8$ and 16 Jy beam^{-1} and $-0.08, 0.08, 0.16, 0.24, 0.48, 1, 2, 4, 8$ and 16 per cent of the peak surface brightness. Darker regions correspond to higher surface brightness. Lower left-hand panel: the map of 3C 223.1 at 610 MHz matched with the resolution of 240 MHz. The contour levels are $-0.08, 0.08, 0.16, 0.24, 0.48, 1, 2, 4, 8$ and 16 per cent of the peak surface brightness. Here again, the darker regions correspond to higher surface brightness. Lower right-hand panel: the distribution of the spectral index, between 240 and 610 MHz, for the source. The spectral index contours are spaced at $-2.4, -1.2$ and 0.6 per cent of the peak spectral index. The lighter regions represent the relatively steep-spectrum regions as compared with the darker regions which represent flat-spectrum regions (although the full range of spectral index is -3.4 to $+1.1$, we have shown only -1.0 to $+0.8$ for clarity). The spectral indices quoted for four regions are determined using integrated flux densities found over a circular region of ~ 5 pixel radius centred at the position of the tails of the arrows shown. The error bars on the spectral index are determined using the error bars on the flux density found at a source-free location using similar sized circular regions, which are ~ 3.0 and $\sim 0.4 \text{ mJy beam}^{-1}$ at 240 and 610 MHz, respectively. These error bars, both spectral indices and flux densities, do not change significantly with increasing or decreasing the size of circle and they also do not change significantly by changing the position of circular region slightly. The maximum possible systematic error in spectral index is either 0.05 across the source or 0.14 for the wings and 0.01 for the active lobes (see Section 4).

Table 2. The total intensity and spectral comparisons for the source and source regions. The total flux densities quoted are given in Jy along with corresponding error bars (1σ). Labels denote: ^athe Large Cambridge interferometer (Ryle 1960); ^bour GMRT measurements; ^cFicarra, Grueff & Tomassetti (1985); ^dthe VLA FIRST survey (Becker, White & Helfand 1995); ^eKellermann et al. (1969); and ^fthe Green Bank, Northern Sky Survey (White & Becker 1992). The last two rows show the best-fitting spectra to the source and source regions: ^glow-frequency (between 240 and 610 MHz) spectral indices; and ^hhigh-frequency (between 1400 and 32 000 MHz) spectral indices (Dennett-Thorpe et al. 2002).

Freq (MHz)	Flux density (Jy)				
	Total	N lobe	W wing	S lobe	E wing
178 ^a	8.7				
240 ^b	8.33 ± 0.41	2.95 ± 0.003	0.18 ± 0.003	3.27 ± 0.003	0.12 ± 0.003
408 ^c	4.72 ± 0.10				
610 ^b	3.56 ± 0.17	1.07 ± 0.001	0.10 ± 0.001	1.20 ± 0.001	0.09 ± 0.001
1400 ^d	1.90 ± 0.28	0.55	0.04	0.63	0.03
2695 ^e	1.23 ± 0.61				
4850 ^f	0.78 ± 0.11				
α^g	-0.91 ± 0.07	-1.08 ± 0.01	-0.62 ± 0.02	-1.08 ± 0.01	-0.37 ± 0.03
α^h	-0.75 ± 0.02	-0.75	-0.66	-0.77	-0.70

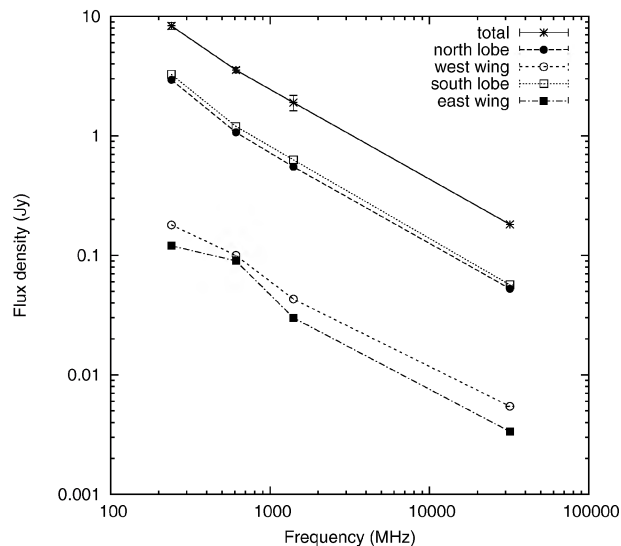


Figure 2. The flux density for the total source, the active lobes and the wings. The 1.4-GHz measurements are from the Faint Images of the Radio Sky at Twenty cm (FIRST) survey (Becker, White & Helfand 1995). The 32-GHz flux densities shown are estimated using the spectral indices in Dennett-Thorpe et al. (2002) applied to the FIRST survey measurements. The error bars on the flux densities for the source regions are $\lesssim 3.0$ mJy.

be introduced due to possible negative depression. The maximum possible depressions close to the source at 240 and 610 MHz are -7.6 and -2.7 mJy beam⁻¹, respectively. This worst case would introduce a maximum error of 0.14 in spectral indices for the wings and 0.01 for the active lobes. Because the observed differences in spectral index at low frequencies are much greater than any of these uncertainties for 3C 223.1, we believe that the observed spectral index features are real.

5 DISCUSSION

Many authors have attempted to explain the unusual structure in X-shaped sources. The first attempt was made by Rees (1978), who suggested that the jet direction precesses due to a realignment caused by the accretion of gas with respect to the central black hole axis. Dennett-Thorpe et al. (2002) discussed four possible scenarios for the formation of such radio morphology: (1) backflow from the active lobes into the wings (Leahy & Williams 1984; Capetti et al. 2002); (2) slow conical precession of the jet axis (Parma, Ekers & Fanti 1985; Mack et al. 1994); (3) reorientation of the jet axis during which flow continues; and (4) reorientation of the jet axis, but with the jet turned off or at greatly reduced power during the change of direction. Merritt & Ekers (2002) suggested another possible scenario, namely the reorientation of the black hole's spin axis due to a minor merger, leading to a sudden flip in the direction of any associated jet. A variant of the Merritt & Ekers (2002) model was suggested by Gopal-Krishna, Biermann & Wiita (2003), where the sources with Z morphology within their X shapes evolve along a Z–X morphological sequence. Presently, most of the observational results seem to prefer possibilities 3 and 4 of Dennett-Thorpe et al. (2002), Merritt & Ekers (2002) or Gopal-Krishna et al. (2003). The key difference between the Dennett-Thorpe et al. (2002) and Merritt & Ekers (2002) reorientation models is in terms of the mechanism of reorientation; the former favoured the disc instability mechanism because of little evidence for a recent merger in their sample, whereas the latter preferred the coalescence scenario. Nevertheless, in these favoured scenarios (and also in other models), the wings are interpreted as relics of past radio jets and the active lobes are interpreted as the newer ones.

Using these radio observations, the spectra at different locations in the source might be used to distinguish between some of the models suggested for these sources. In the simplest picture, the low-surface-brightness wings would have an older population of the electrons, and therefore should have steeper spectral index compared with the active high-surface-brightness radio lobes if the magnetic fields are uniform in the measured regions. However, the spectra of the low-surface-brightness jet (or the wings) being flatter than the active high-surface-brightness jet is opposite to this simple picture.

5.1 Interpretations based on spectral ageing

Below we present some of the assumptions used in the spectral ageing method for estimating the age and discuss what could be modified to explain the above result.

(i) The injection spectral index is assumed to be constant during the active phase of the active galactic nucleus (AGN) and the evolution of the synchrotron spectrum is assumed to be due to the synchrotron losses. One of the favoured scenario for the formation of X-shaped sources is the reorientation of the jet axis (Dennett-Thorpe et al. 2002). It is possible that, along with the reorientation of the jet axis, the injection spectral index also changed. It is then possible to have a flatter spectral index in the wings compared with the active lobes. A similar interpretation was also suggested by Palma et al. (2000) to explain the anomalous spectral index features seen in NVSS 2146+82.

(ii) In classical radio galaxies, it is usually the high-surface-brightness hotspots that consist of a young population of energetic electrons and they are the source of plasma for the low-surface-brightness lobes, which eventually consist of an older population of electrons. In the case of X-shaped sources, the formation of which is yet to be understood, it is possible that this is not the case. Instead, it

is possible that the wings are in the process of becoming new active jets, in which case it is not surprising that they have flatter spectral index compared with the active lobes.

(iii) Reacceleration mechanisms are mainly seen in hotspots and sites undergoing interactions, which needs to be appropriately accounted for while interpreting the evolution of the synchrotron spectrum. The diffuse, low-surface-brightness regions are usually believed to be relaxed systems. It is hard to achieve reacceleration mechanisms in the low-surface-brightness lobes or wings via standard Alfvén waves and Fermi mechanisms. Therefore, it is currently difficult to reconcile the observed spectral indices in the wings and the active lobes, unless there exists an additional exotic reacceleration mechanism.

(iv) Magnetic field strength does not evolve and its distribution is believed to be isotropic, and hence the synchrotron emission is isotropic. Blundell & Rawlings (2000) have questioned this assumption, and have provided an alternative physical picture which could mimic the observed spectral behaviour. They invoke a gradient in magnetic field across the source, together with a curved electron energy spectrum, which would result in spectral indices being different at distinct locations within the source and could possibly explain our observed results.

5.2 X-shaped sources: the merger of two AGNs

We now discuss an alternative scenario, which has not been addressed earlier, for the X-shaped sources.

Although there are several examples of resolved binary AGN systems, examples of unresolved binary AGN systems are unknown. X-shaped sources could be of the latter kind, with two pairs of jets being associated with two unresolved AGNs. An indirect hint of the presence of binary AGNs arises from using *HST* to identify inwardly decreasing surface brightness profiles in the galaxy. This is also found to be so using *N*-body simulations, in which a coalescing binary black hole creates a ‘loss cone’ (displaced matter within a distance which is roughly the separation between the two black holes when they first form a bound pair) around it (Merritt 2004). We have re-analysed the archived *HST* data, and close inspection of the deconvolved brightness profile does not suggest a centrally depressed, nearly flat core. However, this could be due to obscuration of the core by the dusty disc, as suggested by de Koff et al. (1996), and therefore we could not see a signature of the ejection of stars from the core during the hardening of the AGNs undergoing merger.

Future high-resolution, phase-referencing, very-long-baseline-interferometry radio imaging of 3C 223.1 could look for Keplerian orbital motion of some emission component close to black holes, and might be used to detect the presence of binary AGNs containing supermassive black holes (e.g. 3C 66B, Sudou, Iguchi & Murata 2003).

6 CONCLUSIONS

We have presented the lowest-frequency image of 3C 223.1 at 240 MHz. The important consequences of these observations, combined with our 610 MHz observations, are as follows.

(i) The low-surface-brightness lobes (the ‘wings’) have flatter spectra compared with the high-surface-brightness active radio lobes.

(ii) This result is not easily explained in most models of the formation of X-shaped sources.

(iii) Low-frequency, high-resolution radio images for the entire sample of X-shaped sources would be useful in understanding the formation models for these sources. A project using GMRT is in progress and the analysis is in an advanced stage. Our subsequent papers will present the morphological and spectral radio results, and will discuss the results statistically for the whole sample of X-shaped sources.

ACKNOWLEDGMENTS

We thank the staff of the GMRT who have made these observations possible. GMRT is run by the National Centre for Radio Astrophysics of the Tata Institute of Fundamental Research. We also thank the anonymous referee for his/her prompt review of the manuscript and for comments that lead to improvement of the paper. DVL thanks R. Nityananda, K. Subramanian and P. J. Wiita for discussions and several useful comments and S. Ravindranath for helping with *HST* data analysis. This research has made use of the NASA/IPAC Extragalactic Data base which is operated by the Jet Propulsion Laboratory, Caltech, under contract with the NASA, and NASA’s Astrophysics Data System.

REFERENCES

- Ananthakrishnan S., Rao A. P., 2002, in Paul B., Manchanda R. K., eds, Proc. conf., Multi Colour Universe. Tata Inst. Fundam. Res., India, p. 233
- Baars J. W. M., Genzel R., Pauliny-Toth I. I. K., Witzel A., 1977, *A&A*, 61, 99
- Becker R. H., White R. L., Helfand D. J., 1995, *ApJ*, 450, 559
- Blundell K. M., Rawlings S., 2000, *AJ*, 119, 1111
- Black A. R. S., Baum S. A., Leahy J. P., Perley R. A., Riley J. M., Scheuer P. A. G., 1992, *MNRAS*, 256, 186
- Capetti A., Zamfir S., Rossi P., Bodo G., Zanni C., Massaglia S., 2002, *A&A*, 394, 39
- de Koff S., Baum S. A., Sparks W. B., Biretta J., Golombek D., Macchetto F., McCarthy P., Miley G. K., 1996, *ApJS*, 107, 621
- Dennett-Thorpe J., Scheuer P. A. G., Laing R. A., Bridle A. H., Pooley G. G., Reich W., 2002, *MNRAS*, 330, 609
- Fanaroff B. L., Riley J. M., 1974, *MNRAS*, 167, 31P
- Ficarra A., Grueff G., Tomassetti G., 1985, *A&AS*, 59, 255
- Gopal-Krishna, Biermann P. L., Wiita P. J., 2003, *ApJ*, 594, L103
- Kellermann K. I., Pauliny-Toth I. I. K., Williams P. J. S., 1969, *ApJ*, 157, 1
- Leahy J. P., Parma P., 1992 in Roland J., Sol H., Pelletier G., eds, *Extragalactic Radio Sources. From Beams to Jets*, Cambridge University Press, p. 307
- Leahy J. P., Williams A. G., 1984, *MNRAS*, 210, 929
- Mack K.-H., Gregorini L., Parma P., Klein U., 1994, *A&AS*, 103, 157
- Merritt D., 2004, in Ho L. C., ed., *Coevolution of black holes and Galaxies*. Cambridge Univ. Press, Cambridge
- Merritt D., Ekers R. D., 2002, *Sci*, 297, 1310
- Palma C., Bauer F. E., Cotton W. D., Bridle A. H., Majewski S. R., Sarazin C. L., 2000, *AJ*, 119, 2068
- Parma P., Ekers R. D., Fanti R., 1985, *A&AS*, 59, 511
- Rees M. J., 1978, *Nat*, 275, 516
- Ryle M., 1960, *J. Inst. Electron. Eng.*, 6, 14
- Sudou H., Iguchi S., Murata Y., 2003, *Sci*, 300, 1263
- Swarup G., Ananthakrishnan S., Kapahi V. K., Rao A. P., Subrahmanya C. R., Kulkarni V. K., 1991, *Cu. Sc.*, 60, 95 2003, *ApJ* 126, 113
- White R. L., Becker R. H., 1992, *ApJS*, 79, 331

This paper has been typeset from a $\text{\TeX}/\text{\LaTeX}$ file prepared by the author.